

RESEARCH ARTICLE OPEN ACCESS

Artificial Amorphous Interface Matters for Boosting High-Voltage Stable LiCoO₂ Cathode

Jinjin Ma^{1,2} | Yipeng Sun¹ | Xiaozhang Yao² | Haoqi Ren² | Wen Zhang¹ | Jian Peng¹ | Ruizhi Yu² | Ruying Li² | Changhong Wang¹ | Jigang Zhou³ | Xueliang Sun^{1,2}

¹Eastern Institute for Advanced Study, Ningbo Key Laboratory of All-Solid-State Battery, Zhejiang Key Laboratory of All-Solid-State Battery, Ningbo Institute of Digital Twin, Eastern Institute of Technology, Ningbo, Ningbo, China | ²Department of Mechanical and Materials Engineering, University of Western Ontario, London, ON, Canada | ³Canadian Light Source Inc., University of Saskatchewan, Saskatoon, SK, Canada

Correspondence: Yipeng Sun (ypsun@eitech.edu.cn) | Changhong Wang (cwang@eitech.edu.cn) | Jigang Zhou (jigang.zhou@gm.com) | Xueliang Sun (xsun9@uwo.ca)

Received: 2 September 2025 | **Revised:** 30 November 2025 | **Accepted:** 23 December 2025

Keywords: amorphous interface | cathode | ionic conductivity | lithium-ion batteries | structure integrity

ABSTRACT

The energy density of lithium-ion batteries (LIBs) can be improved significantly by elevating the working voltage. Nevertheless, serious issues are generally induced at higher cut-off voltages for LIBs, including structural collapse and oxygen loss on the cathode side. Constructing a stable cathode-electrolyte interface (CEI) is considered as an effective approach to tackle these issues. Previous research has predominantly focused on designing crystallized interfacial structures. This omits the coating materials with other structures that could potentially surpass crystallized counterparts. Herein, the amorphization of the phosphate interface has been designed for high-voltage stable LCO by precisely tailored atomic-level fabrication. The modified LCO cathode exhibits excellent high-voltage rate capability of 142.1 mAh g⁻¹ at 10 C and significantly improved cycling stability with a capacity retention of 83.3% after 200 cycles at 1 C. The outstanding performance attributes to the conformal high-voltage stable interface with favorable Li-ion conducting kinetics at LCO surface. Additionally, synchrotron-based X-ray analysis demonstrates that this amorphous layer helps stabilize lattice oxygen and alleviate the variation in the chemical state and local environment of Co at the deep charging state. This work offers new perspectives and possibilities on interphase engineering toward high-energy and stable LIBs.

1 | Introduction

Increasing output voltage of lithium-ion batteries (LIBs) is one of the most crucial approaches to boost the energy density. However, cathode materials face serious challenges on high cut-off voltage due to the deteriorative interfacial and structural instability [1, 2]. For instance, commercial lithium cobalt oxide (LCO) could almost double its capacity when further increasing its original charging cut-off voltage above 4.2 V, but suffer from poor electrochemical reversibility and catastrophic capacity decay owing to its intrinsic issues [3, 4]. The generation of Li vacancies at elevated voltage distorts the lattice and obstructs the ionic

transport, leading to the gradual collapse of the crystal structure. At deep delithiated stage, the oxidation of lattice oxygen occurs due to the increasing energy level of O 2p, which becomes higher than that of Co t_{2g} [5]. The oxidation phenomenon leads to the generation of oxygen radicals, which attack the electrolyte and cause its decomposition. Moreover, the release of lattice oxygen leads to the formation of irreversible rock-salt phase [6, 7].

To mitigate the critical issues of LCO at elevated voltage, it is essential to achieve a stable cathode-electrolyte interface (CEI) which can alleviate the undesired side reactions between LCO and electrolyte, as well as maintain the crystal structure of LCO

This is an open access article under the terms of the [Creative Commons Attribution-NonCommercial-NoDerivs](#) License, which permits use and distribution in any medium, provided the original work is properly cited, the use is non-commercial and no modifications or adaptations are made.

© 2026 The Author(s). *Advanced Functional Materials* published by Wiley-VCH GmbH

free from irreversible phase transition [5, 8]. Surface modification is reported as one of the most effective strategies to tackle the challenges of LCO in recent years. A variety of interfacial coating layers, such as oxides [9–12], fluorides [13–16], and polymers [17–20], have been studied to understand their effects on the electrochemical behaviors of LCO. It has been discovered that coatings are able to suppress the Co dissolution, reduce the HF attack, stabilize the cathode crystal structure, and mitigate the oxygen release. It is generally considered that an ideal CEI possesses excellent electrochemical stability, favorable electronic/ionic conductivity, conformal coverage, and thin thickness [21, 22].

It is worth noting that previous research has predominantly focused on diverse crystallized coating structures, playing substantial role in terms of performance improvement. Especially, lattice-coherent coating structures receive great attention owing to the structure integrity with cathode [23–25]. However, this omits the coating materials with other structures that could potentially surpass crystallized counterparts with regards to electrochemical performance and synthesizing feasibility. In addition to crystallized coating materials, amorphous materials inherently offer several advantages, including structural flexibility, reduced grain boundary and broader compositional tunability [26], which may overcome the limitations of crystallized coating layers. It is notable that an amorphous layer without any grain boundaries provides isotropic Li-ion diffusion pathways and strengthens the interface between cathode and electrolyte, thereby enhancing electrochemical performance of cathode materials [26, 27]. Furthermore, the precise fabrication of an amorphous interfacial layer to achieve conformal coverage, excellent electrochemical stability, and favorable ionic transportation is of great importance for a high-voltage stable LCO.

Herein, we propose a facile atomic-level interphase amorphization strategy to achieve high-voltage stable LCO. A nanoscale amorphous phosphate layer (lithium zirconium phosphate, abbreviated as LZPO) is fabricated by atomic layer deposition (ALD) with excellent electrochemical stability and favorable ionic transport properties. The amorphous LZPO facilitates LCO with high-voltage rate capability of 142.1 mAh g^{-1} at 10 C and improves the cycling stability with a capacity retention of 83.3% after 200 cycles at 1 C. This ionic conductive LZPO helps LCO cathode to minimize the highly oxidized $\text{O}^{\alpha-}$ ($\alpha < 2$) species in the near-surface region when charged to high potentials and greatly suppresses oxygen loss, which are the keys to maintaining the structural stability of LCO. Moreover, the effectively regulated surface alleviates the evolution of chemical state and local environment of Co in deep charge state. These findings offer new perspectives in designing stable interfaces and pursuing stable high-voltage cathodes.

2 | Results and Discussion

Figure 1a schematically illustrates the vapor phase surface chemistry for fabricating the amorphous phosphate structure. Three compounds containing Li, Zr, and P were selected as ALD precursors, while deionized water was employed as an oxidizer to participate in the self-limiting reaction and realize a single atomic layer of LZPO coating. The composition and thickness

can be precisely tailored by controlling the precursor pulsing doses, pulsing times, and sub-cycles. Details of the deposition procedure are described in the experimental section of Supporting Information. LZPO coatings were deposited on carbon nanotubes (CNTs) for the observation of ALD coating. TEM measurement was conducted to witness the deposition and surface morphology of LZPO coating layer on CNTs. The elemental mapping indicates that Zr, P, and O elements are homogeneously dispersed on CNTs (Figure 1b). Based on ICP analysis on 60-cycle LZPO coated CNTs, the molar ratios of Li, Zr, and P are 5.6: 2.6: 5.9, which corresponds to an approximate LZPO composition of $\text{Li}_{2.2}\text{Zr}_1\text{P}_{2.3}\text{O}_x$.

Figure 1c illustrates the amorphous LZPO coating with 2 cycles (LCO-M2) was uniformly deposited on LCO particle surface with a thickness of around 4 nm. It has been mentioned that ALD is a thin film deposition technique that relies on unique self-limiting surface chemistry reaction route. This deposition process involves the sequential deposition of monolayers, which intrinsically prevents the formation of crystalline grains. Also, its mild deposition temperature makes atoms or molecules with insufficient thermal energy to mobile for forming the long-range and well-ordered lattice structure. These features make it particularly suitable for the successful fabrication of amorphous coating layers with delicate conformality. The successful deposition of LZPO on the surface of LCO was further verified by X-ray absorption near edge structure (XANES) spectra. The Zr L₃-edge spectrum (Figure 1d) shows two features at around 2225 and 2227 eV, which correspond to 2p→4d electron transitions, indicating the majority of Zr^{4+} ions in six-fold coordination [28, 29]. Figure 1e exhibits the P K-edge spectrum of LZPO coating, in which the distinct shoulder on the higher energy side of the white line peak (around 2155 eV) suggests the predominance of Zr–P chemical bond [30]. The scanning electron microscopy (SEM) images indicate the maintained surface morphology of LCO after LZPO coating (Figure S1). X-ray absorption fine structure (XAFS) and pair distribution function (PDF) were applied to probe the local structure and short-range order of LCO and LCO-M2. It should be noted that the R space spectrum obtained by Fourier transform (FT) from the extended X-ray absorption fine structure (EXAFS, Figure 1f) is not phase corrected, resulting in a bond length 0.3 Å lower than the peak position in PDF spectrum [31]. Pristine LCO and LCO-M2 exhibit nearly identical features in the Co K-edge EXAFS R-space spectra. In PDF (Figure S2), two main peaks, between 1 and 3 Å, are well aligned between the cathode with and without coating, revealing unchanged interatomic distances of Co-O and Co-Co. The other main features within 20 Å are almost identical for both LCO and LCO-M2. X-ray diffraction (XRD) was further performed to understand whether the crystal structure of LCO cathode was changed after ALD modification (Figure S3). The XRD patterns of both LCO and LCO-M2 samples show the same features without obvious changes, which displayed an ordered layered structure, corresponding to a hexagonal R $\bar{3}$ m structure. Therefore, the bulk structure of LCO is well maintained during the ALD coating reaction.

To optimize coating thickness, modified LCO cathodes with different coating cycles (1 cycle, 2 cycles and 5 cycles), were denoted as LCO-M1, LCO-M2 and LCO-M5. Coin cells were assembled using commercial carbonate electrolyte and were tested at 1 C between 2.8 and 4.5 V. LCO-M2 delivers the highest specific capacity and shows the best cycling stability (Figure S4).

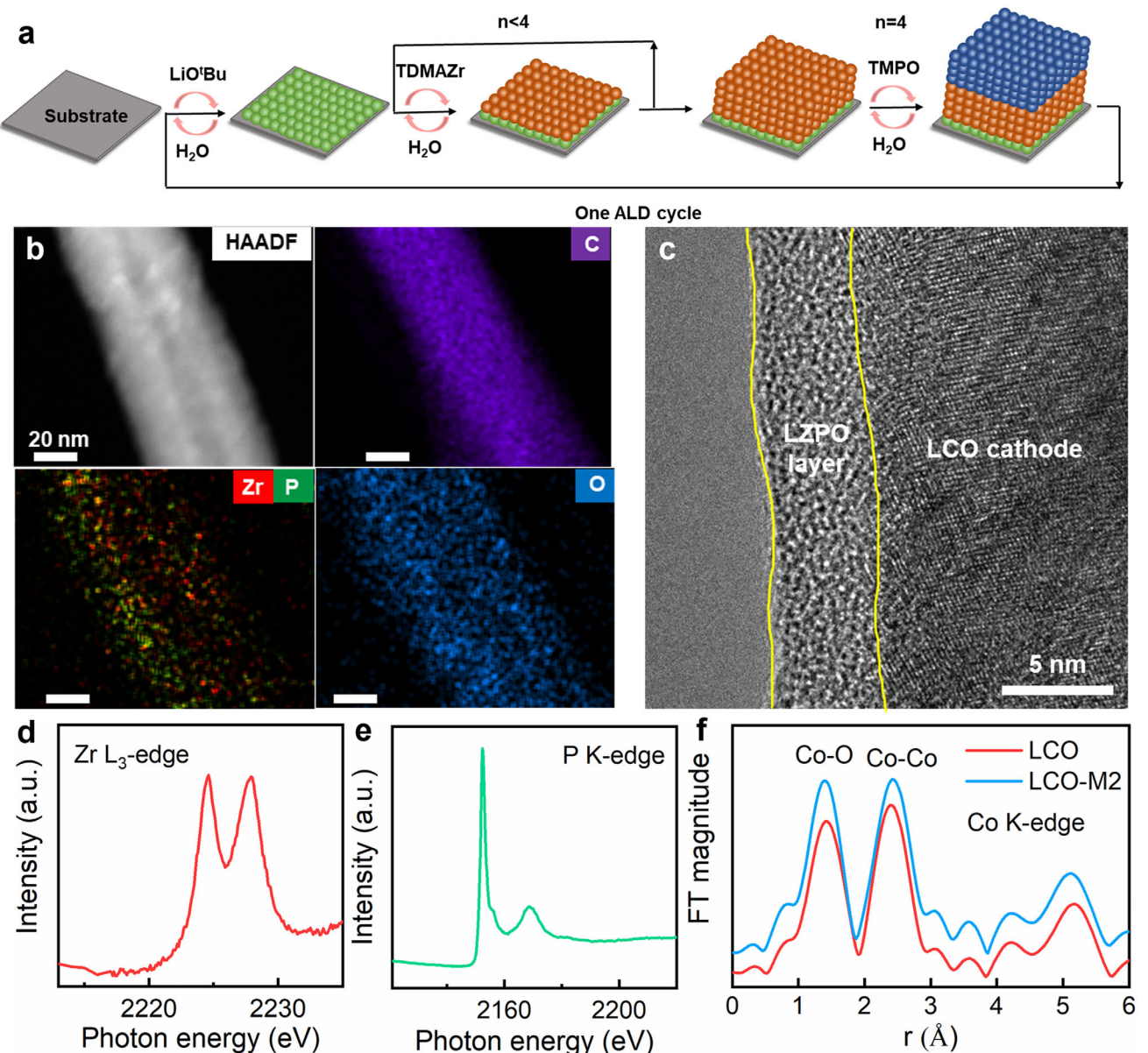


FIGURE 1 | Characterization of lithium zirconium phosphate (LZPO) coating and LZPO film-coated LCO cathode. (a) Illustration of ALD LZPO fabrication process. (b) HAADF image and element mapping of LZPO coated CNTs. (c) TEM image of LZPO coating layer on LCO particle. (d) Zr L_3 -edge XANES and (e) P K-edge XANES of LZPO thin film coated LCO cathode. (f) Co K-edge R-space spectra of pristine LCO and 2 cycles LZPO-coated LCO (LCO-M2).

It might be due to the unoptimized coating layer could either be too thin to prevent side-reactions between cathode the electrolyte or too thick to maintain the fast Li-ion transport on the surficial region. Moreover, the influence of Li content in LZPO coating was tested via adjusting LiO_x sub-cycles. Increasing LiO_x sub-cycle will increase Li content in LZPO coating material. LZPO coating with one cycle of LiO_x shows enhanced performance than further increased Li content (Figure S5), which may be due to the over saturation of Li resource in LZPO coating while depositing more sub-cycles of LiO_x . To comprehensively understand the LZPO coating on high-voltage LCO, the electrochemical performance of pristine LCO and LCO-M2 was compared in Figure 2a–d. The capacity–voltage profile in Figure 2a exhibits a higher discharge capacity of 186.4 mAh g^{-1} for LCO-M2 than 179 mAh g^{-1} for LCO when charging to 4.5 V at 0.1 C. The cycling performance

at different current densities (0.1 C, 0.2 C, 0.5 C, 1 C, 2 C, 5 C, and 10 C) for pristine LCO and LCO-M2 has also been tested and illustrated in Figure 2b. The cell with LCO-M2 exhibits higher discharge capacity at all the current densities, possibly attributed to the good ionic conductivity of the LZPO coating. Especially, LCO-M2 can deliver a capacity of 142.1 mAh g^{-1} at 10 C, better than other reported LCO cathodes with surface modifications based on the crystalline coating structures (summarized in Figure 2c and Table S1). Additionally, LZPO coating significantly enhanced long cycling stability, shown in Figure 2d. Within 2.8–4.5 V, LCO-M2 remains a capacity of 159.2 mAh g^{-1} after 200 cycles with a capacity retention of 83.3%, while pristine LCO dropped to 105.4 mAh g^{-1} only after 100 cycles at 1 C. In the voltage range of 2.8–4.6 V, LCO-M2 can deliver an initial discharge capacity of 223.7 mAh g^{-1} at 1 C and maintain 70.17% of its

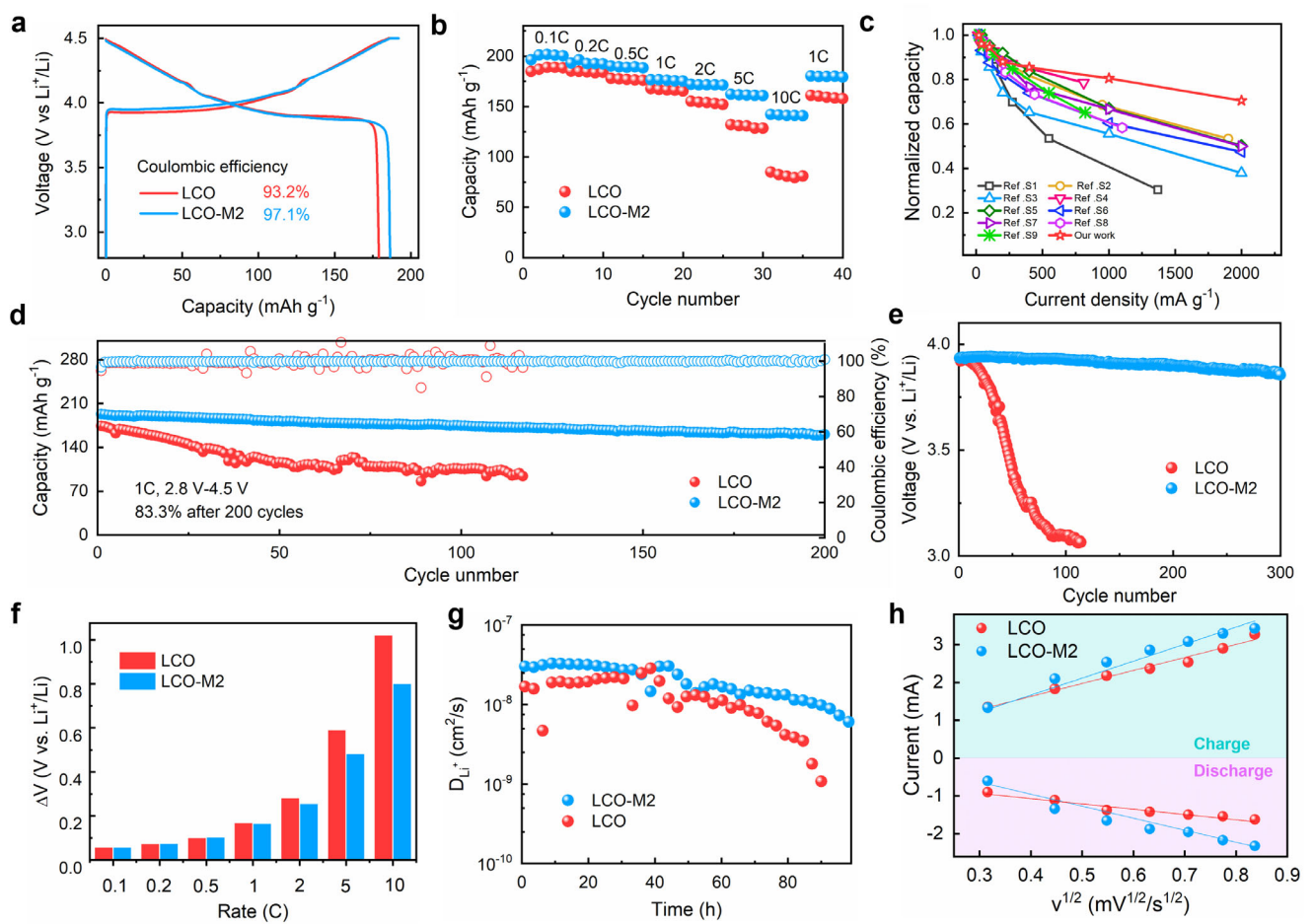


FIGURE 2 | Electrochemical performance of LCO cathode coated by LZPO amorphous thin film. (a) Capacity-voltage profiles of LCO and LCO-M2 in 2.8–4.5 V at 0.1 C. (b) The rate performance of LCO and LCO-M2 in 2.8–4.5 V. (c) The comparison of the rate performance between LCO-M2 and the crystallized coating layers modified LCO cathodes. The references are listed in Table S1. (d) Cycling performance of LCO-M2 in the voltage range of 2.8–4.5 V at 1 C. (e) Discharge voltage variation during cycles. (f) The plot of ΔV as a function of the rate. ΔV is defined as the voltage difference of the charge peak and discharge peak in the dQm/dV curves for quantifying the polarization change. (g) Li-ion diffusivity based on GITT measurement in the discharge of the 60th cycle. (h) The linear relationship between the cathodic peak current and the square root of the scan rate ($v^{1/2}$).

capacity after 100 cycles, whereas LCO can only maintain 44.9% within 74 cycles. When increasing the charging voltage to 4.7 V, LCO-M2 can still maintain a specific capacity of 112.3 mAh g⁻¹, after 100 cycles, sharply in contrast to pristine LCO (13.7 mAh g⁻¹, Figure S6). Remarkably, the obtained discharge capacity of LCO-M2 outperforms the reported results based on a variety of modification methods from literature, as summarized in Table S2.

Lithium-ion diffusion is a critical factor that affects the electrochemical performance of LCO. The effect of LZPO coating on Li^+ diffusion kinetics is qualitatively evaluated via EIS, CV and GITT. The average discharge voltage of LCO-M2 is reduced by 0.08 V, 10 times less than 0.84 V of bare LCO (Figure 2e). This means polarization is significantly alleviated even after long cycles owing to the improved diffusion. More evidence has been provided on the voltage difference between charging and discharging peak ΔV (Figure 2f; Figure S7). It exhibits almost the same values for LCO and LCO-M2 from 0.1 C to 1 C. However, the ΔV value of LCO-M2 is 0.802 V at 10 C, far less than that of LCO (1.021 V), suggesting the reduced polarization after LZPO coating even at high current density. GITT was conducted to

measure the Li^+ -ion diffusion coefficient (Figure 2g and Figure S8). The calculated Li^+ diffusivity (D_{Li^+}) in the 60th discharge showed that the average D_{Li^+} of LCO-M2 was above 10^{-8} S cm⁻¹, significantly higher than that of pristine LCO. The high D_{Li^+} of LCO-M2 significantly maintained electrochemical kinetics and stabilized long-cycling properties. Additionally, the CV testing at different scan rates was presented in Figure S9. The relationship between the apparent lithium-ion diffusion coefficient and the peak current in the CV can be qualified by the Randles-Sevcik equation [32]:

$$I_p = SD^{1/2} v^{1/2}$$

in which I_p represents peak current; S represents surface area of electrode; D represents apparent lithium-ion diffusion coefficient and v represents scan rate. The apparent lithium-ion diffusion coefficient can be evaluated based on the slope of the peak cathodic current (I_p) and the square root of the scan rate ($v^{1/2}$). The larger slope of LCO-M2 after cycling test indicates the maintained efficient paths for Li^+ diffusion at high voltages due to the high-voltage stability of the coating (Figure 2h). Overall, increased surface conductivity significantly improves the Li^+ ions diffusion

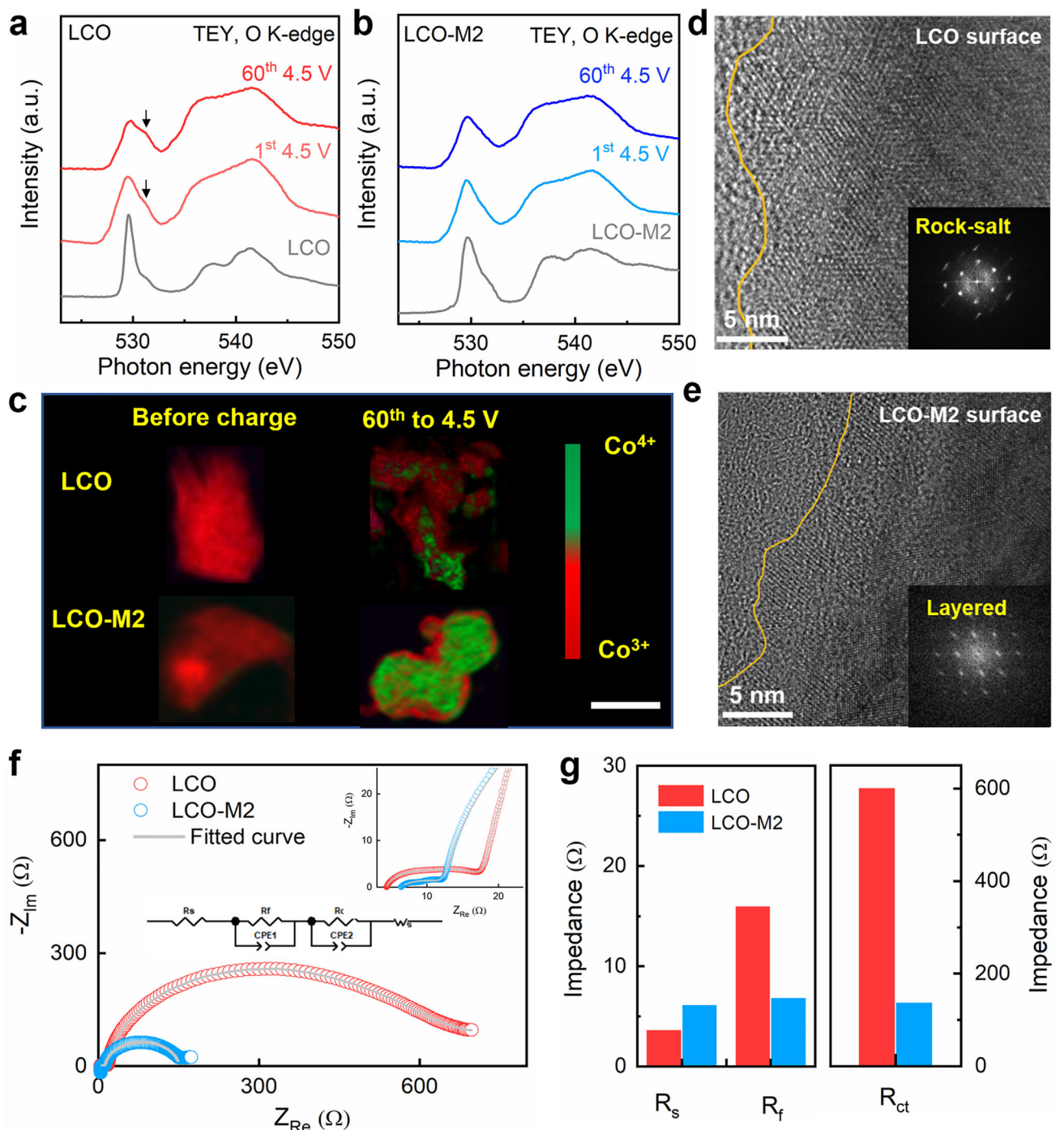


FIGURE 3 | Tracking the oxygen loss and phase transition in the cathodes. O K-edge XANES spectra of (a) LCO and (b) LCO-M2 under TEY mode. (c) Ex situ 2D STXM of pristine LCO and LCO-M2; Scale bar presents 3 μm. HRTEM images of 60th cycled (d) LCO and (e) LCO-M2 at the surficial region. (f) EIS results of the 60th cycled LCO and LCO-M2. (g) Fitted EIS results of bulk electrolyte resistances (R_s), superficial resistance (R_f) and charge transfer resistance (R_{ct}).

and reduces the polarization, thus the rate capability and cycling stability are significantly enhanced.

We carried out XANES under total electron yield (TEY) mode to investigate the oxidation of oxygen ions at the charged cathode surficial region [33–35]. In Figure 3a, a new peak appeared at around 532 eV for pristine LCO indicates an expected $O^{2-} \rightarrow O^{\alpha-}$ ($\alpha < 2$) reaction when charging to 4.5 V. This peak clearly

intensified in the 60th charging process, meaning that oxidation of oxygen ions occurs throughout the whole electrochemical reactions. O K-edge in LCO-M2 shows distinct features compared with the lattice O in LCO, suggesting the chemical state of O in LZPO is different to LCO. O K-edge XANES of LCO-M2 changed subtly after the 60th charging, demonstrating that the oxygen ions indeed remained at –2 valence at the charged particle surface (Figure 3b). The eliminated $O^{2-} \rightarrow O^{\alpha-}$ at the

cathode surface after LZPO modification would greatly alleviate the oxygen migration and oxygen loss at high voltage [36]. It has been reported that oxygen oxidation results in O²⁻ escaping from the LCO lattice structure, and then leads to the Co reduction [37]. The reduced Co ions (Co^{2+/3+}) will migrate to tetrahedral or octahedral sites, accompanied by phase transform from the layered structure into the rock-salt phase [33, 37]. This detrimental phase is ionically and electrically inactive, which is consistent with unstable electrochemical performance. In this work, we applied scanning transmission X-ray microscopy (STXM) for complementary understanding of the Co valence distribution in cathode particles from cycled LCO and LCO-M2 in the 60th charging state with the high spatial resolution (Figure 3c). Co oxidation states were mapped by tracking the whiteline peak positions of the XANES spectra for Co³⁺ (in red) and Co⁴⁺ (in green) (Figure S10). Ideally, the Co should be in the chemical state of Co⁴⁺ upon charging process. Inhomogeneous distributions of Co³⁺ and Co⁴⁺ oxidation states are found to coexist after charging LCO cathodes to 4.5 V. The charged LCO particles are almost fully covered by the reduced Co ions after 60th charging process. Differently, there are very little patches comprising of low-valent (+3) Co ions in red around the LCO-M2 particle edges. To further understand the variation in the valence state of O in the bulk region, O K-edge XANES under FY mode was conducted during different charging states. It is worth mentioning that the integrated intensity in the region of Co_{3d}-O_{2p} (Figure S11) represents the redox reactivity of oxygen [38]. After long cycles, LCO-M2 showed a higher integrated intensity than pristine LCO, indicating LCO-M2 has more Co_{3d}-O_{2p} unoccupied states. This is well consistent with the Co STXM results (Figure 3c), in which Co has a higher oxidation state in the bulk of LCO-M2 than pristine LCO at the 60th charging state. The O K-edge XANES and Co XANES mapping demonstrated that LZPO modification effectively suppressed the oxygen loss and maintained reversibility of Co redox reaction in the charging to high voltage.

The alleviated Co reduction and oxygen loss at high charging cut-off voltage could help stabilize the cathode structure. The SEM images exhibited that pristine LCO cathode has experienced serious pulverization, and significant cracks have been observed inside the particles and along the LCO particle surface, while the surface of cycled LCO-M2 electrode was very smooth without formation of obvious cracks after 100 cycles (Figure S12). The high-resolution transmission electron microscopy (HRTEM) images and Fourier transform patterns in Figure 3d,e additionally confirm that there were random disordered rock-salt domains near the LCO particle surface, while the LCO-M2 particle still maintains ordered layered structure. The stabilized layered phase in LCO-M2 can sustainably promote the Li⁺ diffusion and reduce interior resistance in the battery cycling. From EIS results, the high-frequency region represents the surficial resistance (R_f), while the mid-frequency region represents the charge transfer resistance (R_{ct}) [39, 40]. When charging to 4.5 V, the R_f of LCO and LCO-M2 show a slight increase, and then remain relatively stable in the subsequent discharging process, which is probably due to the evolution of the contact between cathode and electrolyte and the formation of a stable CEI. The pristine LCO shows a huge growth in R_{ct} to 498 Ω, while LCO-M2 cathode slightly increases to 337 Ω (Figure S13). After 60 cycles, the charge transfer resistance R_{ct} of LCO exhibits a larger value compared to

modified LCO (Figure 3f). Also, the surficial resistance R_f of LCO (16.03 Ω) is much higher than that of LCO-M2 (6.861 Ω). Detailed fitting results are listed in Figure 3g. The significantly increased R_{ct} and R_f of LCO indicated much serious solid-liquid side reaction and sluggish charge transfer without LZPO protection during cycling. It is notable that both cathodes exhibit less pronounced Warburg impedance after long cycling. A tiny ‘arc curve’ tail in the low-frequency region is presented in cycled LCO, indicating non-ideal diffusion possibly owing to interfacial and near-surface degradation [23, 41]. Cycled LCO-M2 exhibits a short straight line in the diffusion region, suggesting less deviation from Warburg impedance. These results further demonstrate that the stable cathode structure under LZPO protection significantly maintains the charge transfer kinetics and cell electrochemical performance, as discussed in Figure 2g,h.

As Co is dominantly responsible for the capacity of the LCO cathode, the Co L_{2,3}-edge and Co K-edge are studied from the XAS measurements to track the chemical state and local environment of Co in this work. As shown in Co L-edge XANES TEY spectra (Figure 4a), two features A and B at around 778 and 780 eV correspond to Co²⁺ and Co³⁺, respectively [42]. Co²⁺ is considered as a noticeable feature of Co₃O₄-like phase [36]. In the first charging stage at 4.5 V, Co²⁺ appeared in both pristine LCO and LCO-M2 samples, while this feature became more obvious for LCO and there was no noticeable change for LCO-M2 in the 60th charging stage at 4.5 V. This indicates the more serious phase transition in the pristine LCO cathode surface, which agrees well with the trends that has been observed in the HRTEM and STXM results. The bulk-sensitive Co L-edge XANES fluorescence yield (FY) spectra were also investigated for LCO and LCO-M2. The feature C at around 781 eV (Co⁴⁺) are clearly shown in Figure S14. The higher intensity of Co⁴⁺ in the 60th charging process suggests the better reversibility of LZPO coated cathode, which corresponds to the higher delivered capacity compared with pristine LCO. To alleviate the distortion of FY spectra due to self-absorption, inverse partial fluorescence yield (IPFY) under O K-edge [22, 43] was further performed to investigate Co chemical state (Figure 4b). The decreased intensity of peak A from IPFY compared with FY spectra suggests that the distortion of features from FY has been significantly corrected. The variation in peak A further indicates the formation of Co²⁺ in LCO was earlier than in LCO-M2 and these features exist constantly after the 60th charging process. It is evident that the chemical degradation of LCO cathode has been effectively suppressed by LZPO protection.

Co K-edge XAS measurements were performed to further understand the structural evolution for the 100th cycled LCO and LCO-M2 cathodes. As shown in Figure 4c, it is noticeable that the Co K-edge spectrum of 100th cycled LCO-M2 almost overlaps with that of uncycled sample, suggesting its superior electrochemical reversibility. By sharp contrast, the edge position in the cycled LCO exhibits a prominent leftward shift of 1.5 eV. Moreover, the first derivative of intensity is analyzed to clarify the peak position, where LCO cathode shifts toward lower energy compared to LCO-M2 (Figure 4d). The notably reduced energy position shift for LCO-M2 is probably attributed to the diminished accumulation Co²⁺ containing by-products due to the suppressed buildup of rock-salt Co₃O₄ phase owing to the structure degradation. Extended X-ray absorption fine structure (EXAFS) measurement was carried out to investigate the local

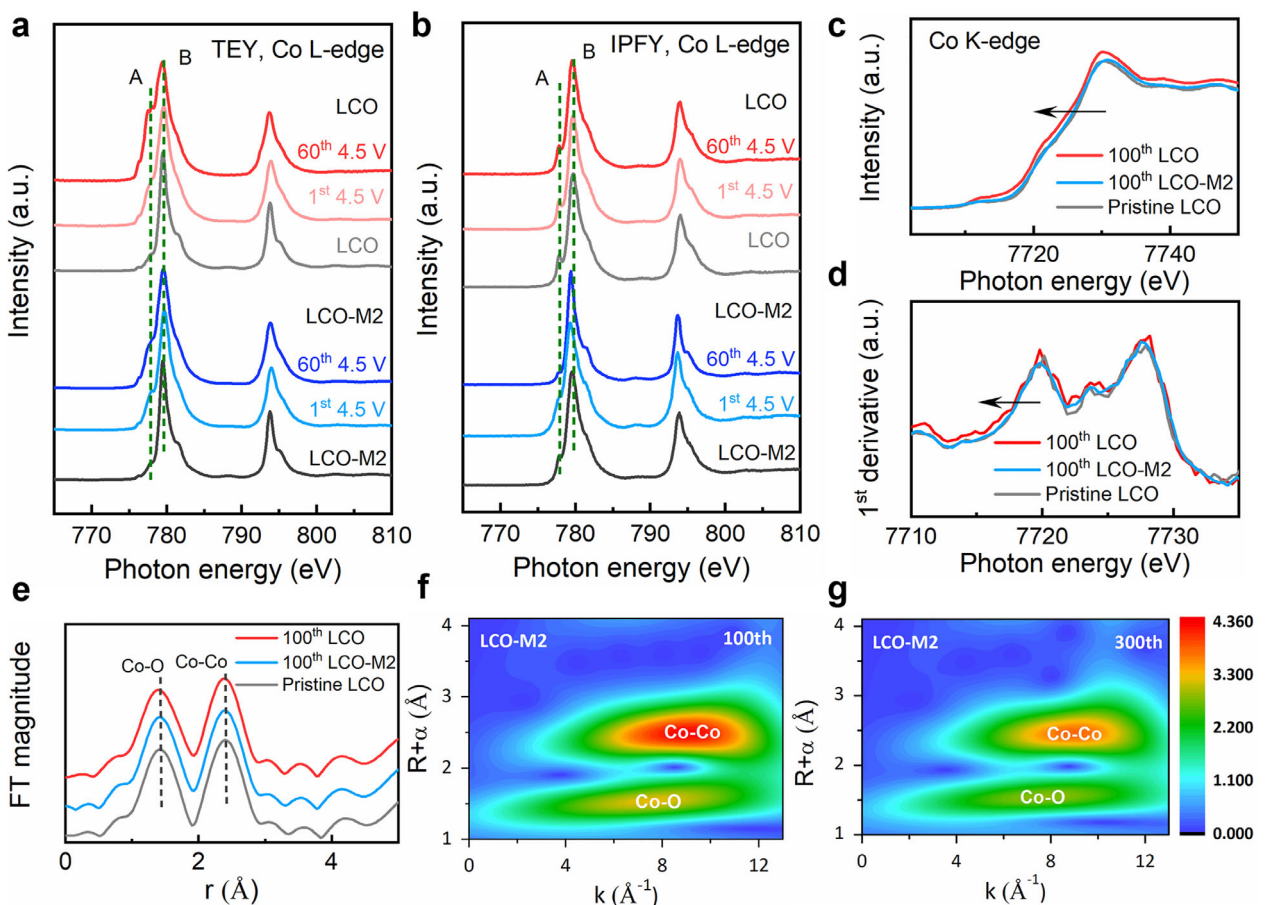


FIGURE 4 | X-ray absorption characterization on the chemical state and local environment of Co. Co L_{2,3}-edge XANES (a) TEY and (b) IPFY spectra of LCO and LCO-M2 cathodes in different charging states compared with uncycled LCO and LCO-M2. (c) Co K-edge XANES spectra of pristine LCO, 100th cycled LCO and 100th cycled LCO-M2. (d) The first derivative intensity of Co K-edge XANES spectra. (e) Co K-edge R-space curves of LCO and LCO-M2 cathodes after 100 cycles. 2D Fourier transformed Co K-edge EXAFS spectra for LCO-M2 cathodes after (f) 100 cycles and (g) 300 cycles.

structures of cathodes and the effects of LZPO coating on the cathode after cycling (Figure 4e). Both the Co-O and Co-Co coordination distances in pristine LCO were shortened after 100 cycles accompanied by the distinctly weakened amplitude, indicating the local structure disorder and Co ions escaping from crystal lattice due to the structure degradation. On the contrary, the interatomic peak shifts are nearly insignificant for the cycled LCO-M2, further demonstrating the upgraded ordering and well-built lattice structure. Synchrotron-based PDF results also suggest the similar results, in which the Co-O and Co-Co coordination distances of cycled LCO cathode are distorted compared to uncycled cathode and cycled LCO-M2 (Figure S15). The 2D contour Fourier transform Co K-edge EXAFS analysis can better distinguish the backscattered atoms and analyze the local environment of Co. Even after 300 cycles, the LCO-M2 still show the unchanged distance and intensity of Co-O and Co-Co, (Figure 4fg), confirming the good local structure stability and reversibility. Overall, serious structure distortion has been found in the LCO cathode due to degradation during electrochemical reaction, while LCO-M2 still maintains its local structure, which can be attributed to LZPO's protective role on the interphase.

To directly compare the protection effects of amorphous and crystalline LZPO coating materials, the LCO cathode with crystallized Li₂Zr(PO₄)₂ coating layer was prepared via ball milling with

pure LCO particles and 1 wt.% Li₂Zr(PO₄)₂ materials, denoted as LCO-C. The energy dispersive X-ray spectrometry (EDS) mapping indicated that the Li₂Zr(PO₄)₂ was dispersed conformally on LCO particle (Figure S16a). Figure S16b illustrates LCO particle is completely covered by Li₂Zr(PO₄)₂ coating. The coating thickness of 3–4 nm with 1 wt% crystallized Li₂Zr(PO₄)₂ layer of the surface region of LCO-C was displayed in Figure S16c, which clearly suggested that Li₂Zr(PO₄)₂ coating layer was attached closely to the lattice of LCO (Figure S16d). It is worth mentioning that LCO-C exhibited improved electrochemical performance compared to pristine LCO (Figure S17). However, LCO-C exhibits a lower discharge capacity at different rates and an unsatisfied long cycling stability than LCO-M2.

XRD was conducted to understand how the crystal structure of LCO cathode changed under crystallized and amorphous LZPO surface modification (Figure S18). LCO-C and LCO-M2 showed the same XRD features, which proved a well-preserved layered cathode structure. After 60 cycles, LCO-C displayed a significant shift of the (003) plane toward a lower angle, suggesting the irreversible structure degradation. In sharp contrast, there was no shift for all the diffraction peaks of cycled LCO-M2 compared with the uncycled cathode, suggesting excellent structural stability after amorphous LZPO coating. HRTEM was further performed on LCO-C to understand the morphology change at the 60th

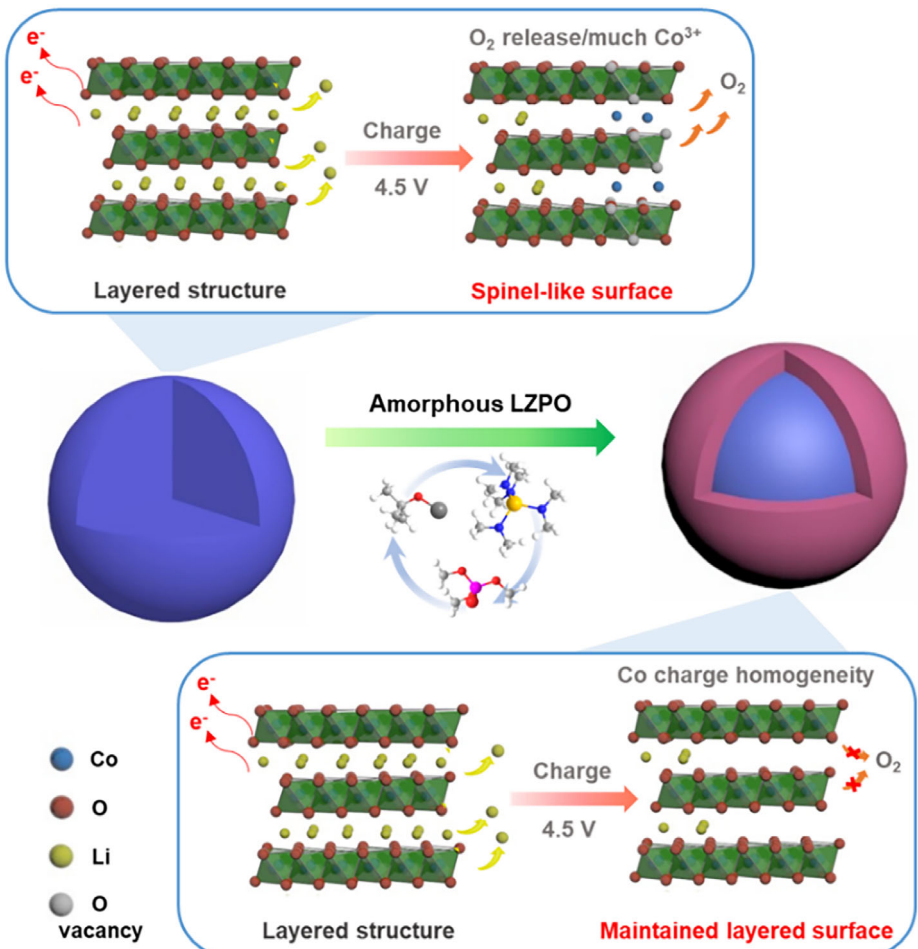


FIGURE 5 | Schematic of ALD enabling LCO cathode with alleviated surface degradation at high voltage.

charging process (Figure S19). Obviously, the spinel-like structure was observed on the surface of LCO-C cathode, corresponding to the irreversible phase transition. Moreover, differential electrochemical mass spectroscopy (DEMS) was employed to detect oxygen release when charging LCO-C and LCO-M2 cathodes to 4.6 V. As shown in Figure S20, clear O₂ evolution (*m/z* = 32) appeared when C-LCO was charged to 4.5 V, suggesting oxygen loss associated with the lattice phase transition, even in the presence of a crystallized LZPO coating. In contrast, no detectable O₂ gas was observed for LCO-M2 up to 4.6 V. This demonstrated that the oxygen release was substantially suppressed by amorphous LZPO coating. In short, ALD fabricated amorphous LZPO coating demonstrates great promise to enhance the electrochemical performance of high-voltage LCO compared to crystallized surface modification owing to the ability to mitigate near-surface irreversible phase transition and maintain structure stability.

To elucidate the mechanism on how the amorphous LZPO layer suppresses surface oxygen oxidation, first-principles calculations were performed and displayed in Figure S21. The charge-density difference at the LCO-LZPO interface shows pronounced charge distribution, where yellow and blue regions correspond to electron accumulation and depletion, respectively. It is shown that electron transfer primarily occurs at the interface, with electrons migrating from the LZPO layer toward the LCO surface.

This interfacial electron enrichment is expected to mitigate the oxidation of surface oxygen species (O²⁻ → O^{α-}, α < 2), thereby inhibiting oxygen release [44, 45]. In addition, partial density of states (PDOS) analysis of interfacial and bulk oxygen reveals that the O 2p orbitals at the interface exhibit fewer high-energy states near the Fermi level (E_f) compared to lattice oxygen [46]. This demonstrated that the amorphous LZPO coating effectively lowers interfacial oxygen activity during electrochemical cycling.

According to the analysis, the mechanism of ALD amorphous LZPO is summarized in Figure 5. Benefiting from the self-limiting chemistry of atomic-level fabrication, the composition and thickness are tailored to construct a robust surface coating layer on LCO. With good interfacial lithium-ion transportation, excellent high-voltage tolerance, and conformal seamless surface coverage, the LZPO layer enables LCO high resistivity of highly oxidized O^{α-} species and alleviates oxygen loss. These functions contribute to the outstanding cycling stability and rate performance at elevated operating voltages.

3 | Conclusion

In summary, we demonstrate the amorphization of phosphate-based surface layer with high ionic conductivity to couple with high voltage LCO by one-step ALD process. It is found that the

LZPO coating greatly suppress the oxygen loss and maintain the reversibility of Co redox reaction. The interfacial ionic transport kinetics have also been dramatically improved based on LZPO surface modification. As a result, a superior rate capability was achieved with a capacity of 142.1 mAh g^{-1} at 10 C and the stable cycling performance was obtained with a capacity retention of 83.3% after 200 cycles at 1 C. Our work opens a new direction to develop a new type of coating material and unfolds new opportunities to design high-voltage cathodes with long lifespan and fast charge capability for LIBs.

Author Contributions

X. Sun, J. Zhou, C. Wang, and Y. Sun supervised the whole project. J. Ma performed the electrochemical testing and STXM analysis for cathodes and wrote the manuscript. Y. Sun tested and processed the XAFS data. X. Yao conducted the TEM characterization. H. Ren carried out the SEM and XRD characterization. W. Zhang and J. Peng conducted DEMS measurement. R. Yu and R. Li participated in the data analysis and discussion.

Acknowledgements

This work was supported by the National Natural Science Foundation of China (Grant Nos. W2441017, 22409103, 92572112), the National Key R&D Program of China (Grant No. 2025YFF0523000) and the “Innovation Yongjiang 2035” Key R&D Program (Grant Nos. 2024Z040, 2025Z063), the Postdoctoral Innovation Talent Support Program (Grant No. BX20240175), the Natural Science and Engineering Research Council of Canada (NSERC), the Canada Research Chair Program (CRC), the Canada Foundation for Innovation (CFI), Ontario Research Fund (ORF), and the University of Western Ontario (UWO). The authors highly appreciate the great support from the beamline scientists of SXRMB (Dr. Mohsen Shakouri and Dr. Qunfeng Xiao), SM (Dr. Jian Wang) beamlines at the Canadian Light Source.

Conflicts of Interest

The authors declare no conflicts of interest.

Data Availability Statement

The data that support the findings of this study are available from the corresponding author upon reasonable request.

References

- J. Xiang, Y. Wei, Y. Zhong, et al., “Building Practical High-Voltage Cathode Materials for Lithium-Ion Batteries,” *Advanced Materials* 34 (2022): 2200912, <https://doi.org/10.1002/adma.202200912>.
- Y. You and A. Manthiram, “Progress in High-Voltage Cathode Materials for Rechargeable Sodium-Ion Batteries,” *Advanced Energy Materials* 8 (2018): 1701785, <https://doi.org/10.1002/aenm.201701785>.
- K. Wang, J. Wan, Y. Xiang, et al., “Recent Advances and Historical Developments of High Voltage Lithium Cobalt Oxide Materials for Rechargeable Li-Ion Batteries,” *Journal of Power Sources* 460 (2020): 228062, <https://doi.org/10.1016/j.jpowsour.2020.228062>.
- Q. Liu, X. Su, D. Lei, et al., “Approaching the Capacity Limit of Lithium Cobalt Oxide in Lithium Ion Batteries via Lanthanum and Aluminium Doping,” *Nature Energy* 3 (2018): 936, <https://doi.org/10.1038/s41560-018-0180-6>.
- C. Lin, J. Li, Z.-W. Yin, et al., “Structural Understanding for High-Voltage Stabilization of Lithium Cobalt Oxide,” *Advanced Materials* 36 (2024): 2307404, <https://doi.org/10.1002/adma.202307404>.
- M. Cai, Y. Dong, M. Xie, et al., “Stalling Oxygen Evolution in High-Voltage Cathodes by Lanthurization,” *Nature Energy* 8 (2023): 159–168, <https://doi.org/10.1038/s41560-022-01179-3>.
- C. Sun, X. Liao, F. Xia, et al., “High-Voltage Cycling Induced Thermal Vulnerability in LiCoO₂ Cathode: Cation Loss and Oxygen Release Driven by Oxygen Vacancy Migration,” *ACS Nano* 14 (2020): 6181–6190, <https://doi.org/10.1021/acsnano.0c02237>.
- Z. Chen, Y. Qin, K. Amine, and Y. K. Sun, “Role of Surface Coating on Cathode Materials for Lithium-Ion Batteries,” *Journal of Materials Chemistry* 20 (2010): 7606–7612, <https://doi.org/10.1039/c0jm00154f>.
- S. He, A. Wei, W. Li, et al., “Al-Ti-Oxide Coated LiCoO₂ Cathode Material with Enhanced Electrochemical Performance at a High Cutoff Charge Potential of 4.5 V,” *Journal of Alloys and Compounds* 799 (2019): 137–146, <https://doi.org/10.1016/j.jallcom.2019.05.165>.
- Y. J. Kim, H. Kim, B. Kim, et al., “Electrochemical Stability of Thin-Film LiCoO₂ Cathodes by Aluminum-Oxide Coating,” *Chemistry of Materials* 15 (2003): 1505–1511, <https://doi.org/10.1021/cm0201403>.
- S.-J. Sim, S.-H. Lee, B.-S. Jin, and H.-S. Kim, “Effects of Lithium Tungsten Oxide Coating on LiNi_{0.90}Co_{0.05}Mn_{0.05}O₂ Cathode Material for Lithium-ion Batteries,” *Journal of Power Sources* 481 (2021): 229037, <https://doi.org/10.1016/j.jpowsour.2020.229037>.
- M. Zan, S. Weng, H. Yang, et al., “Conformal Coating of a High-Voltage Spinel to Stabilize LiCoO₂ at 4.6 V,” *ACS Applied Materials & Interfaces* 15 (2023): 5326–5335, <https://doi.org/10.1021/acsami.2c21006>.
- J. Qian, L. Liu, J. Yang, et al., “Electrochemical Surface Passivation of LiCoO₂ Particles at Ultrahigh Voltage and Its Applications in Lithium-Based Batteries,” *Nature Communications* 9 (2018): 4918, <https://doi.org/10.1038/s41467-018-07296-6>.
- J. S. Park, A. U. Mane, J. W. Elam, and J. R. Croy, “Amorphous Metal Fluoride Passivation Coatings Prepared by Atomic Layer Deposition on LiCoO₂ for Li-Ion Batteries,” *Chemistry of Materials* 27 (2015): 1917–1920, <https://doi.org/10.1021/acs.chemmater.5b00603>.
- C. Lu, H. Wu, Y. Zhang, et al., “Cerium Fluoride Coated Layered Oxide Li_{1.2}Mn_{0.54}Ni_{0.13}Co_{0.13}O₂ as Cathode Materials with Improved Electrochemical Performance for Lithium Ion Batteries,” *Journal of Power Sources* 267 (2014): 682–691, <https://doi.org/10.1016/j.jpowsour.2014.05.122>.
- S. Dai, G. Yan, L. Wang, et al., “Enhanced Electrochemical Performance and Thermal Properties of Ni-Rich LiNi_{0.8}Co_{0.1}Mn_{0.1}O₂ Cathode Material via CaF₂ Coating,” *Journal of Electroanalytical Chemistry* 847 (2019): 113197, <https://doi.org/10.1016/j.jelechem.2019.113197>.
- H. Wang, J. Lin, X. Zhang, et al., “Improved Electrochemical Performance of LiNi_{0.8}Co_{0.1}Mn_{0.1}O₂ Cathode Materials Induced by a Facile Polymer Coating for Lithium-Ion Batteries,” *ACS Applied Energy Materials* 4 (2021): 6205–6213, <https://doi.org/10.1021/acsam.1c00982>.
- Z. Lin, C. Lin, F. Chen, R. Yu, and Y. Xia, “In Situ Construction of a Polymer Coating Layer on the LiNi_{0.8}Co_{0.1}Mn_{0.1}O₂ Cathode for High-Performance Lithium-Ion Batteries,” *ACS Applied Materials & Interfaces* 16 (2024): 10692–10702, <https://doi.org/10.1021/acsami.3c17742>.
- Z. Li, J. Miao, W. Hu, et al., “Stabilizing the Oxide Cathode/Sulfide Solid Electrolyte Interface via a Novel Polyaniline Coating Prepared by Ball Milling,” *Chemical Communications* 59 (2023): 5627–5630, <https://doi.org/10.1039/D3CC00722G>.
- S. H. Ju, I.-S. Kang, Y.-S. Lee, et al., “Improvement of the Cycling Performance of LiNi_{0.6}Co_{0.2}Mn_{0.2}O₂ Cathode Active Materials by a Dual-Conductive Polymer Coating,” *ACS Applied Materials & Interfaces* 6 (2014): 2546–2552, <https://doi.org/10.1021/am404965p>.
- J. Ma, Y. Sun, D. Wu, et al., “Highly Stabilized Ni-Rich Cathodes Enabled by Artificially Reversing Naturally-Formed Interface,” *Advanced Energy Materials* 15 (2025): 2403150, <https://doi.org/10.1002/aenm.202403150>.
- Y. Sun, J. Ma, D. Wu, et al., “A Breathable Inorganic–Organic Interface for Fabricating a Crack-Free Nickel-Rich Cathode with Long-

- Term Stability," *Energy & Environmental Science* 17 (2024): 5124–5136, <https://doi.org/10.1039/D4EE01254B>.
23. Y. Wang, Q. Zhang, Z.-C. Xue, et al., "An In Situ Formed Surface Coating Layer Enabling LiCoO₂ with Stable 4.6 V High-Voltage Cycle Performances," *Advanced Energy Materials* 10 (2020): 2001413, <https://doi.org/10.1002/aenm.202001413>.
 24. W. Huang, Q. Zhao, M. Zhang, et al., "Surface Design with Cation and Anion Dual Gradient Stabilizes High-Voltage LiCoO₂," *Advanced Energy Materials* 12 (2022): 2200813, <https://doi.org/10.1002/aenm.202200813>.
 25. T. Cheng, Z. Ma, R. Qian, et al., "Achieving Stable Cycling of LiCoO₂ at 4.6 V by Multilayer Surface Modification," *Advanced Functional Materials* 31 (2021): 2001974, <https://doi.org/10.1002/adfm.202001974>.
 26. A. Chandra, A. Bhatt, and A. Chandra, "Ion Conduction in Superionic Glassy Electrolytes: an Overview," *Journal of Materials Science & Technology* 29 (2013): 193–208, <https://doi.org/10.1016/j.jmst.2013.01.005>.
 27. J. Luo, B. Guo, N. Li, et al., "Conductive Binary Li Borate Glass Coating for Improved Ni-Rich Positive Electrode in Sulfide-Based All-Solid-State Li Batteries," *Nature Communications* 16 (2025): 9462, <https://doi.org/10.1038/s41467-025-64532-6>.
 28. C. Patzig, T. Höche, Y. Hu, et al., "Zr Coordination Change during Crystallization of MgO-Al₂O₃-SiO₂-ZrO₂ Glass Ceramics," *Journal of Non-Crystalline Solids* 384 (2014): 47–54, <https://doi.org/10.1016/j.jnoncrysol.2013.04.014>.
 29. S. Seidel, C. Patzig, W. Wisniewski, et al., "Characterizing the Residual Glass in a MgO/Al₂O₃/SiO₂/ZrO₂/Y₂O₃ Glass-Ceramic," *Scientific Reports* 6 (2016): 34965, <https://doi.org/10.1038/srep34965>.
 30. L. Luo, Y. Ma, R. L. Sanders, C. Xu, J. Li, and S. C. B. Myneni, "Phosphorus Speciation and Transformation in Long-Term Fertilized Soil: Evidence from Chemical Fractionation and P K-Edge XANES Spectroscopy," *Nutrient Cycling in Agroecosystems* 107 (2017): 215–226, <https://doi.org/10.1007/s10705-017-9830-5>.
 31. W. Hua, J. Zhang, S. Wang, et al., "Long-Range Cationic Disordering Induces Two Distinct Degradation Pathways in Co-Free ni-Rich Layered Cathodes," *Angewandte Chemie International Edition* 62 (2023): 202214880, <https://doi.org/10.1002/anie.202214880>.
 32. T. Mu, S. Lou, N. G. Holmes, et al., "Reversible Silicon Anodes with Long Cycles by Multifunctional Volumetric Buffer Layers," *ACS Applied Materials & Interfaces* 13 (2021): 4093, <https://doi.org/10.1021/acsami.0c21455>.
 33. S.-M. Bak, Z. Shadike, R. Lin, X. Yu, and X.-Q. Yang, "In Situ/Operando Synchrotron-Based X-Ray Techniques for Lithium-Ion Battery Research," *NPG Asia Materials* 10 (2018): 563–580, <https://doi.org/10.1038/s41427-018-0056-z>.
 34. X. Liu, D. Wang, G. Liu, et al., "Distinct Charge Dynamics in Battery Electrodes Revealed by In Situ and Operando Soft X-Ray Spectroscopy," *Nature Communications* 4 (2013): 2568, <https://doi.org/10.1038/ncomms3568>.
 35. F. Frati, M. O. J. Y. Hunault, and F. M. F. de Groot, "Oxygen K-Edge X-Ray Absorption Spectra," *Chemical Reviews* 120 (2020): 4056–4110, <https://doi.org/10.1021/acs.chemrev.9b00439>.
 36. Z. Zhu, H. Wang, Y. Li, et al., "A Surface Se-Substituted LiCo[O_{2-δ} Se_δ] Cathode with Ultrastable High-Voltage Cycling in Pouch Full-Cells," *Advanced Materials* 32 (2020): 2005182, <https://doi.org/10.1002/adma.202005182>.
 37. M. Yoon, Y. Dong, Y. Yoo, et al., "Unveiling Nickel Chemistry in Stabilizing High-Voltage Cobalt-Rich Cathodes for Lithium-Ion Batteries," *Advanced Functional Materials* 30 (2020): 1907903, <https://doi.org/10.1002/adfm.201907903>.
 38. C. Tian, D. Nordlund, H. L. Xin, et al., "Depth-Dependent Redox Behavior of LiNi_{0.6}Mn_{0.2}Co_{0.2}O₂," *Journal of The Electrochemical Society* 165 (2018): A696, <https://doi.org/10.1149/2.1021803jes>.
 39. H.-J. Guo, Y. Sun, Y. Zhao, et al., "Surface Degradation of Single-Crystalline Ni-Rich Cathode and Regulation Mechanism by Atomic Layer Deposition in Solid-State Lithium Batteries," *Angewandte Chemie International Edition* 61 (2022): 202211626, <https://doi.org/10.1002/anie.202211626>.
 40. W. Liu, X. Li, Y. Hao, et al., "Functional Passivation Interface of LiNi_{0.8}Co_{0.1}Mn_{0.1}O₂ toward Superior Lithium Storage," *Advanced Functional Materials* 31 (2021): 2008301, <https://doi.org/10.1002/adfm.202008301>.
 41. J. Huang, "Diffusion Impedance of Electroactive Materials, Electrolytic Solutions and Porous Electrodes: Warburg Impedance and beyond," *Electrochimica Acta* 281 (2018): 170–188, <https://doi.org/10.1016/j.electacta.2018.05.136>.
 42. S. Xu, X. Tan, W. Ding, et al., "Promoting Surface Electric Conductivity for High-Rate LiCoO₂," *Angewandte Chemie International Edition* 62 (2023): 202218595, <https://doi.org/10.1002/anie.202218595>.
 43. S. Yang, D. Wang, G. Liang, et al., "Soft X-ray XANES Studies of Various Phases Related to LiFePO₄ Based Cathode Materials," *Energy & Environmental Science* 5 (2012): 7007, <https://doi.org/10.1039/c2ee03445j>.
 44. X. A. Zhou, F. Zhang, X. Fu, et al., "Utilizing Fast Ion Conductor for Single-Crystal Ni-Rich Cathodes to Achieve Dual-Functional Modification of Conductor Network Constructing and Near-Surface Doping," *Energy Storage Materials* 52 (2022): 19–28, <https://doi.org/10.1016/j.ensm.2022.07.029>.
 45. Q. Jiang, M. Li, J. Li, et al., "LiF-Rich Cathode Electrolyte Interphases Homogenizing Li⁺ Fluxes toward Stable Interface in Li-Rich Mn-Based Cathodes," *Advanced Materials* 37 (2025): 2417620, <https://doi.org/10.1002/adma.202417620>.
 46. X. Yang, C. Wang, P. Yan, et al., "Pushing Lithium Cobalt Oxides to 4.7 V by Lattice-Matched Interfacial Engineering," *Advanced Energy Materials* 12 (2022): 2200197, <https://doi.org/10.1002/aenm.202200197>.

Supporting Information

Additional supporting information can be found online in the Supporting Information section.

Supporting File: adfm73840-sup-0001-SuppMat.docx.